

A Theory of transmission spectroscopy of planetary winds: Spectral-line saturation and limits on mass-loss inference

Leonardos Gkouvelis¹ *

Instituto de Astrofísica de Andalucía (IAA-CSIC), Glorieta de la Astronomía s/n, E-18008 Granada, Spain

Received January 22, 2026

ABSTRACT

Transmission spectroscopy is a key technique in the characterization of exoplanet atmospheres and has been widely applied to planets undergoing hydrodynamic escape. While a robust analytic theory exists for transmission spectra of hydrostatic atmospheres, the corresponding interpretation for escaping atmospheres has so far relied on numerical modeling, despite the growing number of observations of planetary winds. In this work, we develop a theory of transmission spectroscopy in hydrodynamically escaping atmospheres by coupling the standard transmission geometry to a steady-state, spherically symmetric, isothermal outflow. This approach yields closed-form expressions for the chord optical depth and effective transit radius of a planetary wind and allows the optical depth inversion problem to be examined.

The analytic solution reveals that transmission spectroscopy of planetary winds naturally separates into two regimes. In an opacity-limited regime, transmission depths retain sensitivity to the atmospheric mass-loss rate. Beyond a critical threshold, however, spectral-line cores become saturated and no longer provide a unique constraint on the mass flux. This transition is marked by a sharp analytic boundary of the form $\sigma(\lambda) \dot{M} \leq C_{\text{sat}}$, where C_{sat} is a constant set by the thermodynamic and geometric properties of the wind. This condition specifies when the inversion between transmission depth and mass-loss rate admits a real solution. Once it is violated, the effective transit radius is no longer controlled by opacity or mass loss, but by the geometric extent of the absorbing wind.

These results demonstrate that spectral-line saturation in transmission spectroscopy corresponds to a fundamental loss of invertibility between absorption and atmospheric mass loss, rather than a gradual weakening of sensitivity. The theory provides a physically transparent explanation for why strong transmission line cores, such as the He triplet or Ly α , often fail to constrain mass-loss rates, while weaker lines and line wings remain diagnostic.

Key words. planets and satellites: atmospheres – techniques: spectroscopic – methods: analytical – atmospheric escape

1. Introduction

One of the key techniques on which exoplanet atmospheric characterization relies is transmission spectroscopy. During a primary transit, a fraction of the stellar radiation passes through the planetary atmosphere, where it is selectively absorbed or scattered depending on wavelength and atmospheric composition. As a result, the effective planetary radius inferred from transit observations varies with wavelength. This wavelength-dependent modulation of the transit depth encodes information about atmospheric composition, structure, and opacity sources (Brown 2001). Currently, transmission spectra are routinely obtained and interpreted for a wide range of exoplanets, from hot Jupiters to smaller and cooler planets, using both space- and ground-based facilities (e.g., Espinoza et al. 2024; Steinrueck et al. 2025).

While transmission theory in a broader context was developed early in Earth and planetary sciences, its application to the observational geometry of transiting exoplanets was first presented by Seager & Sasselov (2000). That work identified that atmospheric opacity controls the apparent transit radius and provided a qualitative scaling linking opacity, atmospheric scale height, and transit depth. Later, a closed-form analytic solution was derived by Lecavelier Des Etangs et al. (2008), who showed that, under the assumptions of a hydrostatic and isothermal atmosphere, the effective planetary radius scales logarithmically with opacity as $R_p(\lambda) \sim H \ln \kappa(\lambda)$ where H is the atmospheric

scale height and $\kappa(\lambda)$ is the wavelength-dependent opacity. This logarithmic scaling has served as a canonical result for more than two decades and has provided valuable intuition for the interpretation of transmission spectra. More recently, Gkouvelis (2025) derived a generalized closed-form expression that accounts for pressure-dependent opacity, modifying the classical scaling to $R_p(\lambda) \sim \frac{H}{1+n(\lambda)} \ln \kappa_0(\lambda)$, where n is the power-law exponent describing the pressure dependence of the opacity and κ_0 is a reference opacity. All analytic transmission theories of this kind rely on a common set of assumptions, namely hydrostatic equilibrium, an isothermal atmosphere, and the absence of strong compositional gradients along the transit chord. In addition, well known degeneracies affect the normalization of hydrostatic transmission spectra, limiting the unique retrieval of absolute atmospheric properties (Benneke & Seager 2012; de Wit & Seager 2013). Together, these results provide a robust theoretical framework for building intuition and interpreting transmission spectra of stable, hydrostatic atmospheres.

Nevertheless, a significant fraction of the known exoplanet population resides in a non-hydrostatic regime, commonly referred to as a planetary wind (Watson et al. 1981; Owen 2019), whose onset and long-term persistence can strongly influence the volatile inventory, atmospheric evolution, and potential habitability of rocky planets (Gkouvelis et al. 2025). Under conditions of rapid atmospheric escape, the upper atmosphere is no longer in hydrostatic balance but instead undergoes hydrodynamic outflow, continuously losing mass to space. Transmission spectroscopy

* Corresponding author: e-mail: gkouvelis@iaa.es

has been the primary observational tool for studying this process, mainly through targeted spectral lines with large absorption cross sections that probe atmospheric layers where the outflow is established and, in some cases, extends beyond the Roche lobe (e.g., Ly α , He I 1083 nm; Bourrier et al. 2016; Oklopčić & Hirata 2018).

To date, the interpretation of these observations has relied on numerical models of hydrodynamic escape. One recurring result of such studies is that the cores of strong spectral lines rapidly become insensitive to the mass-loss rate, such that they primarily encode the geometric extent of the absorbing atmosphere rather than the magnitude of the mass flux (Allan & Vidotto 2019; Linssen et al. 2022; Dos Santos et al. 2022). Recent work has highlighted that strong transmission lines, particularly Ly α , do not primarily probe atmospheric mass-loss rates but are instead controlled by geometric and ionization constraints set by the outflow and the stellar environment (Owen et al. 2023).

In contrast, information about the hydrodynamic flow is typically carried by the wings of spectral lines, which remain sensitive to the atmospheric column density and velocity structure (Ballabio & Owen 2025; Lampón et al. 2023). This distinction has so far emerged empirically from numerical modeling, rather than from an analytic transmission framework.

In this work, we couple the standard transmission geometry to an isothermal, spherically symmetric, steady-state hydrodynamic outflow and derive a closed-form expression for the effective transit radius of planetary winds. For wavelengths that probe the atmospheric flow, the analytic solution provides a useful approximation to the transmission spectrum and offers physical insight into its dependence on opacity, temperature, and mass-loss rate. The analytic framework reveals a fundamental limitation of transmission spectroscopy in escaping atmospheres. We show that the mapping between transmission depth and atmospheric mass loss exists only over a restricted range of parameters. Beyond a critical threshold, strong spectral lines become saturated in such a way that the inversion between absorption and mass loss is no longer unique. In this regime, the effective transit radius is set primarily by the geometric extent of the absorbing wind rather than by the mass flux itself. This behavior provides a physical explanation for why the cores of strong transmission lines are often insensitive to mass-loss rates, while diagnostic information about the hydrodynamic flow is gained from weaker lines and in the wings of strong transitions.

This work is organized as follows. In Sect. 2, we describe the hydrodynamic outflow model and derive analytic expressions for the chord optical depth and effective transit radius in a steady-state planetary wind. In Sect. 3, we analyze the properties and domain of validity of the analytic solution and identify the regimes in which the inversion between transmission depth and mass-loss rate breaks down. In Sect. 4, we compare the analytic predictions to numerical transmission spectra and discuss the physical interpretation of saturated and opacity-limited regimes. Finally, Sect. 5 summarizes the main results and their implications for the interpretation of transmission observations of escaping exoplanet atmospheres.

2. Analytic derivation

2.1. Physical assumptions

We will examine the planetary winds assuming a steady-state, spherically symmetric and isothermal flow, which has the mathematical formulation of the Parker wind solution for the Solar wind (Parker (1958); Lamers & Cassinelli (1999)).

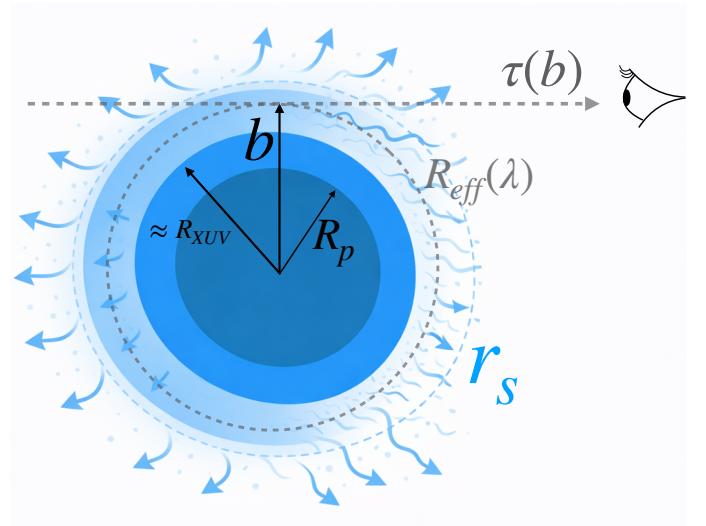


Fig. 1. Geometry of transmission spectroscopy in a planetary wind. A planet of radius R_p is surrounded by a bound hydrostatic atmosphere and an outer hydrodynamically escaping region. Stellar rays intersect the atmosphere along chords of impact parameter b , accumulating a wavelength-dependent slant optical depth $\tau(b)$ along the line of sight toward the observer. The effective transit radius $R_{\text{eff}}(\lambda)$ is defined by the impact parameter for which $\tau(b)$ reaches the reference value τ_* . The dashed blue circle marks the sonic radius r_s and the approximate location of the XUV photosphere, R_{XUV} , is also indicated.

Combining the momentum equation, the mass conservation and the isothermal equation of state we derive the Parker wind equation

$$\left(v^2 - c_s^2\right) \frac{1}{v} \frac{dv}{dr} = \frac{2c_s^2}{r} - \frac{GM_p}{r^2}. \quad (1)$$

The *sonic radius* r_s is defined by the condition $v(r_s) = c_s$. Requiring Eq. (1) to be regular at $r = r_s$ gives

$$r_s = \frac{GM_p}{2c_s^2}. \quad (2)$$

The transonic Parker solution can be written in implicit form as

$$\left(\frac{v}{c_s}\right)^2 - \ln\left[\left(\frac{v}{c_s}\right)^2\right] = 4 \ln\left(\frac{r}{r_s}\right) + 4 \frac{r_s}{r} - 3. \quad (3)$$

Solving for $n(r)$ in the mass conservation equation we have the density profile in the radial axis:

$$n(r) = n_s \left(\frac{r_s}{r}\right)^2 \frac{c_s}{v(r)}. \quad (4)$$

2.2. Transit geometry

We now consider a ray of starlight passing at an impact parameter b (measured from the planetary center). Along the line-of-sight coordinate x , the radial coordinate is

$$r^2 = x^2 + b^2, \quad (5)$$

so that the monochromatic chord optical depth at wavelength λ is

$$\tau(b, \lambda) = 2 \int_{r=b}^{+\infty} \sigma(\lambda) n(r) \frac{r}{\sqrt{r^2 - b^2}} dr. \quad (6)$$

The transmission geometry and the main characteristic radii of the flow are illustrated in Fig. 1. Substituting Eq. (4) into the optical depth gives

$$\tau(b, \lambda) = 2\sigma(\lambda) n_s c_s r_s^2 \int_b^{+\infty} \frac{dr}{v(r) r \sqrt{r^2 - b^2}}. \quad (7)$$

This is the exact chord optical depth in a Parker wind, expressed in terms of the velocity profile $v(r)$ and the sonic-point parameters (r_s, n_s).

In order to keep the analytical tractability, we now approximate this integral in the subsonic region of the Parker wind. The geometric kernel $1/\sqrt{r^2 - b^2}$ peaks strongly near the tangent point $r = b$, so the main contribution to the integral comes from a narrow region around $r \approx b$. This approximation is analogous to the tangent-point treatment commonly adopted in analytic transmission spectroscopy, where the chord optical depth is dominated by a narrow region around the point of closest approach and slowly varying quantities may be evaluated locally (e.g. Lecavelier Des Etangs et al. 2008; de Wit & Seager 2013). In this region, the wind speed varies slowly compared to the geometric factor, and we can approximate $v(r) \approx v(b)$. With this approximation, $v(b)$ is constant with respect to the integration variable r , so that we can factor it out, Eq. (7) becomes

$$\tau(b, \lambda) \simeq \frac{2\sigma(\lambda) n_s c_s r_s^2}{v(b)} \int_b^{+\infty} \frac{dr}{r \sqrt{r^2 - b^2}}. \quad (8)$$

The remaining integral is purely geometrical and can be evaluated analytically. One finds

$$\int_b^{+\infty} \frac{dr}{r \sqrt{r^2 - b^2}} = \frac{\pi}{2b}. \quad (9)$$

Inserting Eq. (9) into Eq. (8), we obtain

$$\tau(b, \lambda) \simeq \frac{2\sigma(\lambda) n_s c_s r_s^2}{v(b)} \frac{\pi}{2b} = \frac{\pi \sigma(\lambda) n_s c_s r_s^2}{b v(b)}. \quad (10)$$

Equation (10) is a general expression for the chord optical depth in a Parker wind, valid in the approximation that the wind speed is nearly constant over the narrow region around the tangent point $r \approx b$.

2.3. Subsonic approximation

In the subsonic region $r \ll r_s$, the isothermal Parker wind admits a simple asymptotic expression for the velocity (see, e.g., Parker 1958). Starting from the implicit relation (3), one finds that for $v \ll c_s$ the velocity can be written as

$$v(r) \simeq c_s e^{3/2} \left(\frac{r_s}{r}\right)^2 \exp\left(-2\frac{r_s}{r}\right), \quad (11)$$

which is valid for radii well below the sonic point, $r \ll r_s$. The numerical prefactor in Eq. 11 depends on the normalization of the transonic solution and is accurate up to a factor of order unity, which does not affect the scaling relations or the qualitative results derived below. A comparison between the exact Parker solution and the subsonic asymptotic approximation is shown in Fig. 2.

Evaluating Eq. (11) at the tangent point $r = b$ and substituting Eq. (11) into Eq. (10) yields

$$\tau(b, \lambda) \simeq \frac{\pi \sigma(\lambda) n_s c_s r_s^2}{b v(b)} = \pi \sigma(\lambda) n_s e^{-3/2} b \exp\left(2\frac{r_s}{b}\right). \quad (12)$$

For later convenience, we define a wavelength-dependent prefactor

$$A(\lambda) \equiv \pi \sigma(\lambda) n_s e^{-3/2}, \quad (13)$$

so that Eq. (12) can be written compactly as

$$\tau(b, \lambda) \simeq A(\lambda) b \exp\left(2\frac{r_s}{b}\right), \quad (b \ll r_s). \quad (14)$$

An example of the resulting chord optical depth profiles for different ultraviolet bands is shown in Fig. 3.

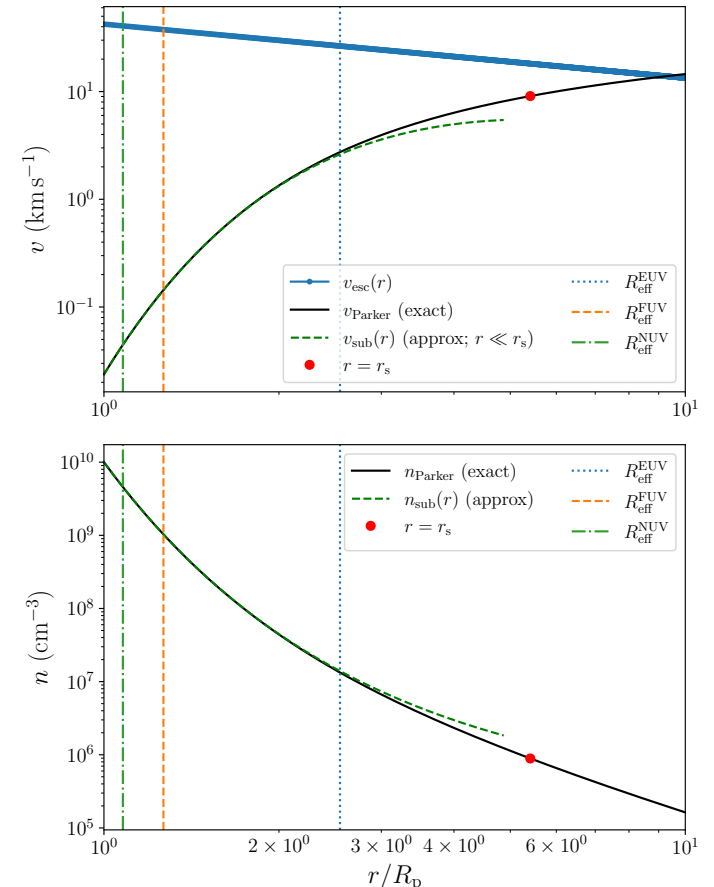


Fig. 2. Radial velocity and density profiles of the Parker wind for the hot Jupiter HD 209458 b. With black solid lines we show the profiles as calculated by the Parker wind formulation while in dashed green we show the subsonic approximation (see Section 2). For comparison, we overplot the radii where the optical depth of the NUV, FUV, EUV are reaching unity, $\tau \approx 1$.

Following, we relate the sonic density to the mass loss rate. With our assumptions the mass loss rate is written as

$$\dot{M} = 4\pi r^2 \rho(r) v(r), \quad (15)$$

Solving for n_s gives and substituting into Eq. (13), the prefactor $A(\lambda)$ can be written directly in terms of the mass-loss rate:

$$A(\lambda) = \pi \sigma(\lambda) e^{-3/2} \frac{\dot{M}}{4\pi \mu m_p c_s r_s^2} = \frac{\sigma(\lambda) \dot{M}}{4 e^{3/2} \mu m_p c_s r_s^2}. \quad (16)$$

2.4. Effective transit radius and Lambert-W solution

In the standard definition, the effective transit radius $R_{\text{eff}}(\lambda)$ is obtained from the total obscured area,

$$R_{\text{eff}}^2(\lambda) = R_0^2 + 2 \int_{R_0}^{+\infty} [1 - e^{-\tau(b, \lambda)}] b \, db, \quad (17)$$

where R_0 is a reference radius (Lecavelier Des Etangs et al. (2008); Gkouvelis (2025)). When $\tau(b, \lambda)$ is a steep function of b , the transmission can be approximated by a sharp transition in opacity. This step-function approximation is standard in transmission theory when the chord optical depth varies rapidly with impact parameter (e.g. Lecavelier Des Etangs et al. 2008; Brown 2001). In this regime it is a good approximation to treat the transmission as a sharp transition at an impact parameter $b_*(\lambda)$ where the chord optical depth reaches a reference value $\tau_* \sim \mathcal{O}(1)$ (common choices are $\tau_* = 1$ or $\tau_* \approx 0.56$ (e.g. Lecavelier Des Etangs et al. 2008)). To leading order in this step-function approximation the effective radius is $R_{\text{eff}}(\lambda) \approx b_*(\lambda)$, where b_* is defined implicitly by $\tau(b_*, \lambda) = \tau_*$.

Combining this condition with the subsonic Parker expression (Eq. (14)), we obtain

$$\tau_* = A(\lambda) b_* \exp\left(2 \frac{r_s}{b_*}\right), \quad (18)$$

or equivalently

$$D(\lambda) \equiv \frac{\tau_*}{A(\lambda)} = b_* \exp\left(2 \frac{r_s}{b_*}\right), \quad (19)$$

where $D(\lambda)$ has dimensions of length. Finally we can solve for b_* in closed form using the Lambert-W function (Corless et al. (1996)).

We define $y \equiv -2r_s/b_*$, so that $b_* = -2r_s/y$. Substituting into Eq. (19) gives $D = (-2r_s/y)e^{-y}$, and rearranging yields

$$y e^y = -\frac{2r_s}{D(\lambda)}. \quad (20)$$

By definition of the Lambert-W function, this implies

$$y = W\left(-\frac{2r_s}{D(\lambda)}\right). \quad (21)$$

Using $b_* = -2r_s/y$, we obtain

$$b_*(\lambda) = -\frac{2r_s}{W(-2r_s/D(\lambda))}. \quad (22)$$

To leading order in the step-function approximation, the effective transit radius is

$$R_{\text{eff}}(\lambda) \approx b_*(\lambda) = -\frac{2r_s}{W(-2r_s/D(\lambda))}. \quad (23)$$

Using $D(\lambda) = \tau_*/A(\lambda)$ and the definition of $A(\lambda)$ (Eq. (16)), we obtain

$$R_{\text{eff}}(\lambda) \approx -\frac{2r_s}{W\left[-\frac{\sigma(\lambda) \dot{M}}{2 e^{3/2} \tau_* \mu m_p c_s r_s}\right]} \quad (24)$$

Equation (24) is a closed-form expression for the effective transit radius of a steady state isothermal flow in terms of the sonic radius r_s , sound speed c_s , mass-loss rate \dot{M} , mean molecular weight μ , and the wavelength-dependent cross section $\sigma(\lambda)$. The Lambert-W solution branch determines the physically relevant solution and is discussed in Section 3.1.

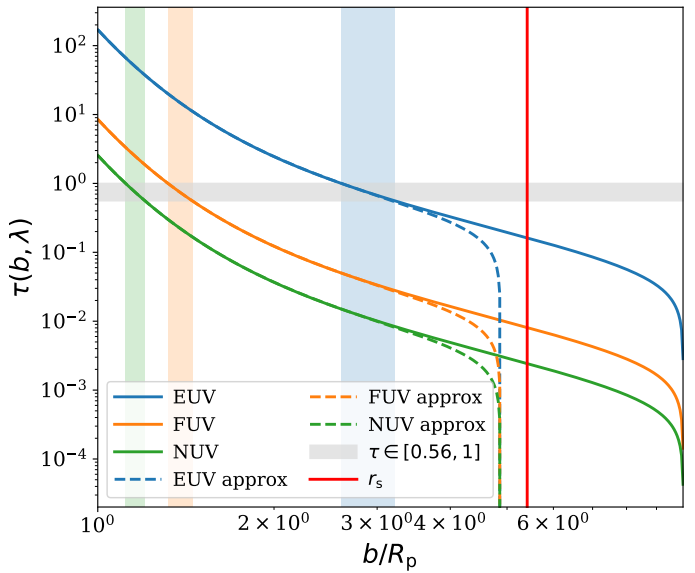


Fig. 3. Optical depth as a function of planet radius for EUV, FUV and NUV wavelength bands as well as approximations for the same bands overplotted. With shaded stripes we show the range $\tau = 0.56\text{--}1$ expressed in terms of the corresponding planet radii for the ultraviolet bands shown.

3. Validity, branches, and saturation boundary

The effective transit radius is obtained by inverting the condition $\tau(b, \lambda) = \tau_*$. This inversion is mathematically equivalent to solving a Lambert-W equation. Whether this equation admits a real solution determines whether transmission spectroscopy provides a unique mapping between absorption depth and atmospheric mass loss. We thus demonstrate that this mapping exists only below a sharp threshold in $\sigma(\lambda) \dot{M}$, and derive this threshold explicitly.

3.1. Lambert-W branches and the physical solution

We now discuss the regime of validity of Eq. (24) and identify the Lambert-W branch that yields a physically meaningful solution in the subsonic region.

The Lambert-W function is defined implicitly by $W(z) e^{W(z)} = z$. For real arguments z , the function has a single real branch $W_0(z)$ for $z \geq 0$, two real branches $W_0(z)$ and $W_{-1}(z)$ for $-1/e \leq z < 0$, and only complex values for $z < -1/e$ (Corless et al. 1996). On the interval $-1/e \leq z < 0$, the principal branch satisfies $-1 \leq W_0(z) < 0$, while the lower branch satisfies $W_{-1}(z) \leq -1$.

For our application, it is convenient to define

$$z(\lambda) \equiv -\frac{\sigma(\lambda) \dot{M}}{2 e^{3/2} \tau_* \mu m_p c_s r_s}, \quad (25)$$

so that Eq. (24) becomes

$$R_{\text{eff}}(\lambda) \approx -\frac{2r_s}{W(z(\lambda))}. \quad (26)$$

Since $\sigma(\lambda) > 0$ and $\dot{M} > 0$, we have $z(\lambda) < 0$ for all wavelengths.

The derivation leading to Eq. (26) assumes that the effective radius lies deep in the subsonic region of the Parker wind, $R_{\text{eff}}(\lambda) \ll r_s$. Introducing

$$y \equiv -\frac{2r_s}{R_{\text{eff}}}, \quad (27)$$

we have $y = W(z(\lambda))$ and $R_{\text{eff}} = -2r_s/y$. The subsonic requirement $R_{\text{eff}} \ll r_s$ implies $|y| \gg 2$, i.e. the solution of $y e^y = z(\lambda)$ must have large negative magnitude. On $-1/e \leq z < 0$, the two real branches behave differently:

- (i) On the principal branch $W_0(z)$, $-1 \leq W_0(z) < 0$, hence $|y| \lesssim 1$ and $R_{\text{eff}} \gtrsim 2r_s$, inconsistent with $R_{\text{eff}} \ll r_s$.
- (ii) On the lower branch $W_{-1}(z)$, $W_{-1}(z) \leq -1$ and $|W_{-1}(z)| \rightarrow \infty$ as $z \rightarrow 0^-$, implying $|y| \gg 1$ and thus $R_{\text{eff}} \ll 2r_s$, consistent with the subsonic approximation.

We therefore conclude that, within the regime where the subsonic Parker approximation is valid and $z(\lambda) \in [-1/e, 0]$, the physically relevant solution is obtained by choosing the W_{-1} branch:

$$R_{\text{eff}}(\lambda) \approx -\frac{2r_s}{W_{-1}(z(\lambda))}, \quad -\frac{1}{e} \leq z(\lambda) < 0 \quad (28)$$

3.2. Real versus complex solutions and the onset of saturation

For $z(\lambda) < -1/e$, the Lambert–W function has no real values, and Eq. (26) yields a complex R_{eff} that has no direct geometric interpretation. In practice, a complex solution is best interpreted as a diagnostic that one (or more) assumptions entering the analytic inversion have broken down. In the present context, the most relevant interpretation is that the optical-depth criterion $\tau(b, \lambda) = \tau_*$ cannot be satisfied at any b within the subsonic regime because the line is saturated: the chord optical depth exceeds τ_* for all grazing chords that remain in the region where the subsonic approximation applies.

Equivalently, the real-domain condition $z(\lambda) \geq -1/e$ defines a sharp boundary in (σ, \dot{M}) space beyond which the analytic inversion ceases to exist as a real-valued mapping.

3.3. A single dimensionless control parameter and a quantitative validity boundary

The analytic expression for the effective transit radius in a Parker wind, Eq. (28), depends on wavelength only through the product of opacity and mass-loss rate. This motivates defining a dimensionless control parameter

$$\chi(\lambda) \equiv \frac{\sigma(\lambda) \dot{M}}{\mu m_p c_s r_s}, \quad (29)$$

such that

$$z(\lambda) = -\frac{\chi(\lambda)}{2e^{3/2}\tau_*}. \quad (30)$$

The analytic solution exists only for real values on the W_{-1} branch, requiring

$$-\frac{1}{e} \leq z(\lambda) < 0, \quad (31)$$

which is equivalent to an upper bound on $\sigma(\lambda) \dot{M}$:

$$\sigma(\lambda) \dot{M} \leq C_{\text{sat}} \quad (32)$$

where we define $C_{\text{sat}} = 2e^{1/2}\tau_* \mu m_p c_s r_s$. This inequality is the quantitative saturation boundary: when it is satisfied, the inversion between absorption and effective transit radius is real-valued and well defined; when it is violated, the corresponding wavelength lies in a saturation-limited regime in which the analytic inversion breaks down. This analytic saturation boundary and the two transmission regimes are illustrated quantitatively in Fig. 6 utilizing HD 209458 b as an example.

3.4. Limitations of the asymptotic expansion

One may formally expand the Lambert–W function for small $|z|$ as

$$W(z) = z - z^2 + \frac{3}{2}z^3 + \mathcal{O}(z^4), \quad (33)$$

which yields a simple approximate scaling of R_{eff} with $\sigma(\lambda)$ and n_s . However, the series (33) is an expansion around $z = 0$ on the principal branch W_0 , where $W(z) \rightarrow 0$ as $z \rightarrow 0$. Because $W_0(z) \in [-1, 0)$ for $z \in [-1/e, 0)$, this would imply $R_{\text{eff}} \gtrsim 2r_s$, i.e. outside the subsonic region where our Parker asymptotics were derived.

By contrast, on the physically relevant branch W_{-1} one has $W_{-1}(z) \rightarrow -\infty$ as $z \rightarrow 0^-$, and the appropriate asymptotic is logarithmic rather than a power series (e.g. Corless et al. 1996). Consequently, the small- $|z|$ expansion (33) is mathematically correct but not self-consistent for the physical regime of interest ($R_{\text{eff}} \ll r_s$). For quantitative work, we therefore recommend using Eq. (28) with the W_{-1} branch and checking *a posteriori* that $R_{\text{eff}}(\lambda) \ll r_s$ for the parameters of interest.

4. Physical interpretation and synthetic spectra

4.1. Analytic transmission synthetic spectra of planetary winds

Setup and numerical framework. We now test the analytic model for non-hydrostatic atmospheres by computing synthetic transmission spectra. To trace the upper atmosphere and thus the hydrodynamic flow, we focus on wavelength regions with large absorption cross sections. Ultraviolet wavelengths are particularly well suited for this purpose, especially for broadband coverage.

In Fig. 4 we present synthetic transmission spectra for the hot Jupiter HD 209458 b, a benchmark system that is well studied observationally and known to undergo hydrodynamic atmospheric escape (Vidal-Madjar et al. 2003, 2004; Murray-Clay et al. 2009). We compute spectra in the ultraviolet range ($\lambda \approx 15–180$ nm) for comparison between a hydrostatic (upper panel) and a hydrodynamic Parker-wind scenario (lower panel). The numerical spectra are computed following Appendix A. Planetary and atmospheric parameters are adopted from representative literature values (e.g. Koskinen et al. 2010, 2013). Ultraviolet photoabsorption cross sections are compiled from multiple sources (Heays et al. 2017; Gkouvelis et al. 2018; Chubb et al. 2024; Gkouvelis et al. 2024), and references therein.

Failure of hydrostatic transmission intuition. The hydrostatic calculation (upper panel of Fig. 4) is included only as a baseline that illustrates what ultraviolet opacities would imply under the assumptions of hydrostatic transmission theory. The resulting spectral morphology differs qualitatively from the wind case: once the atmosphere is not in hydrostatic balance, the mapping between opacity, structure, and transit depth is fundamentally altered. This demonstrates that the physical intuition built from analytic transmission theory for hydrostatic atmospheres does not carry over to the planetary-wind regime.

Analytic–numerical comparison and saturation. In the lower panel of Fig. 4, the black curve shows the numerical transmission spectrum obtained by line-by-line integration through the full Parker wind density profile (Eq. 4). The red curve shows the

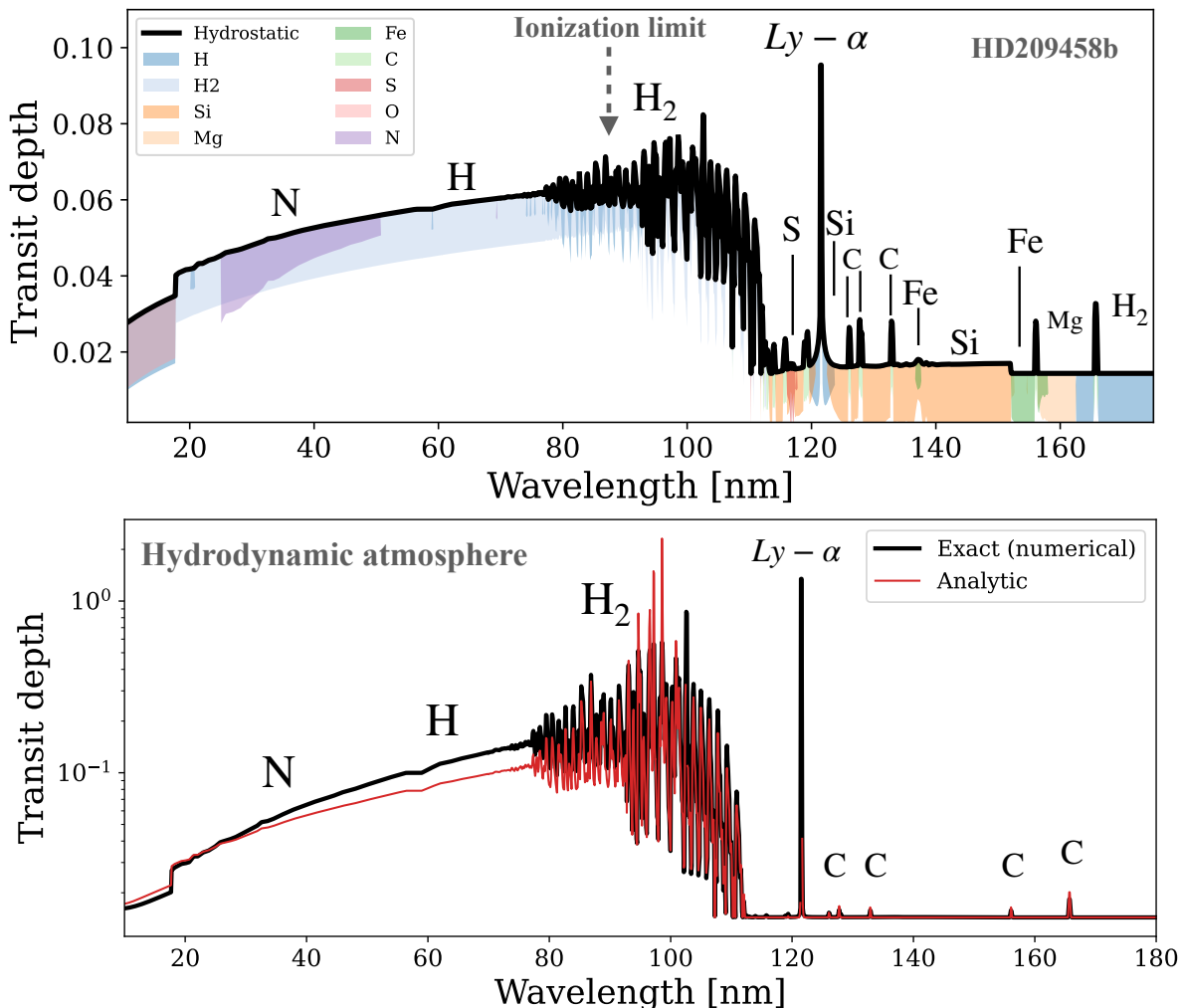


Fig. 4. Up: Transmission spectrum of HD209458b under the hydrostatic/stable thermosphere hypothetical scenario. With shaded regions we indicate the dominant absorption species at each wavelength. Bottom: Comparison of HD209458b hydrodynamic atmosphere's transmission spectrum from numerical integration including line broadening effects from bulk flow and thermal motion, compared to the analytic model derived in Eq. (28).

analytic prediction from Eq. (28). The overall agreement confirms that the analytic solution captures the dominant physics of transmission through a hydrodynamically escaping atmosphere in the regime where the subsonic and step-function approximations apply.

At several wavelengths, however, the analytic solution does not admit a real-valued Lambert-W solution. A characteristic example is the Ly α line core. In the numerical model, the effective radius reaches very large values, as expected for a strongly saturated resonance line. In contrast, the analytic inversion fails because the real-domain condition in Eq. (28) is violated, i.e. $z(\lambda) < -1/e$. The numerical spectrum remains well defined in this regime: it is the analytic inversion between the optical-depth criterion and the effective radius that breaks down, not the underlying radiative-transfer calculation.

This connects directly to the saturation boundary derived in Sect. 3.3. Wavelengths for which Eq. (32) is satisfied correspond to an opacity-limited regime in which R_{eff} remains sensitive to \dot{M} and other physical parameters. Wavelengths for which the inequality is violated lie in a saturation-limited regime: the optical depth exceeds the adopted threshold along all relevant grazing chords, and the mapping between absorption depth and mass loss is no longer invertible. In this sense, saturation is not merely a

gradual reduction in sensitivity, but a sharp loss of invertibility that follows from the analytic structure of the solution.

Expressed in this way, the analytic Parker-wind transmission spectrum highlights that the observable extent of an escaping atmosphere is determined by the interplay between opacity and mass flux, rather than by pressure normalization alone. The sonic radius provides the natural geometric scale controlling the extent of the optically thick region. In Fig. 5 we show the fraction of wavelengths in the ultraviolet that satisfy the real-domain condition $-1/e \leq z(\lambda) < 0$, i.e. the fraction of wavelength points where the analytic inversion remains valid, across a range of mass-loss rates.

5. Discussion

5.1. Information content of transmission spectra in planetary winds

The analytic framework developed in this work shows that transmission spectroscopy of hydrodynamically escaping atmospheres is fundamentally governed by the mathematical structure of the optical depth inversion problem. When the argument of the Lambert-W function remains within its real-valued domain, the effective transit radius is a single-valued and monotonic func-

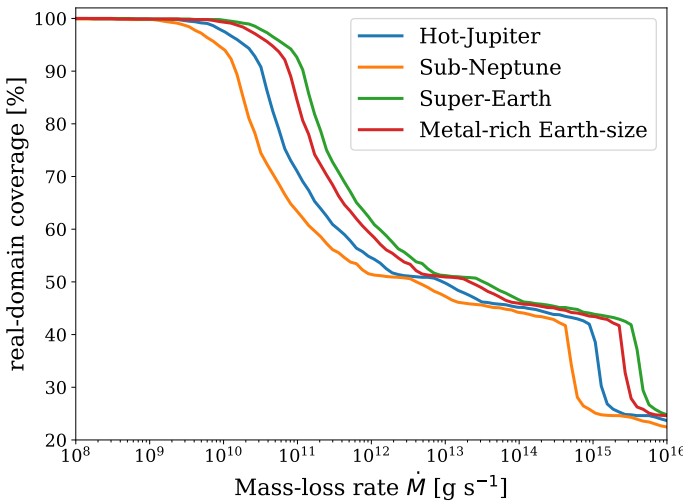


Fig. 5. We define the analytic coverage as the fraction of wavelength points for which the Lambert-W argument satisfies $-1/e \leq z(\lambda) < 0$, ensuring a real-valued effective transit radius.

tion of the product $\sigma(\lambda)\dot{M}$, and the transmission spectrum is *opacity-limited*. In this regime, variations in mass-loss rate, temperature, mean molecular weight, or absorber abundance lead to measurable changes in the transit depth, and the analytic solution accurately reproduces numerical radiative-transfer calculations.

Once the real-domain condition is violated, the inversion ceases to exist as a real-valued mapping. This defines a sharp transition to a *saturation-limited* regime, in which the optical depth along all relevant grazing chords exceeds the reference threshold τ_* . In this case, further increases in opacity or mass flux do not lead to a unique increase in the effective transit radius. This saturation regime reflects a failure of the analytic inversion, not of radiative transfer itself: fully numerical transmission spectra remain well defined and continuous in this limit. Transmission spectroscopy therefore loses its ability to uniquely constrain the atmospheric column density or the mass-loss rate at those wavelengths.

This behavior provides a natural explanation for the long-standing result from numerical models that the cores of strong resonance lines (e.g., Ly α , He I 1083 nm, H α) are often insensitive to \dot{M} , while diagnostic information is preferentially carried by weaker transitions and by the wings of strong lines. In the wings, the optical depth remains below the saturation boundary, the analytic inversion remains well behaved, and the effective radius retains sensitivity to the atmospheric density structure.

From an observational perspective, this implies that transmission spectra should not be interpreted uniformly across wavelength. Instead, spectral regions should be classified according to whether they lie in the opacity-limited or saturation-limited regime. Only the former admit a unique mapping between absorption depth and physical escape parameters.

5.2. Geometric nature of saturated line cores

In the saturation-limited regime, the Lambert-W solution approaches the branch point and the effective transit radius asymptotically converges to

$$R_{\text{eff}} \rightarrow 2r_s, \quad (34)$$

where

$$r_s = \frac{GM_p}{2c_s^2} \quad (35)$$

is the sonic radius of the Parker wind. This saturation scale depends only on the planetary gravitational potential and the atmospheric temperature through the sound speed, and is independent of both the absorption cross section and the mass-loss rate. The observable absorption depth in saturated line cores therefore reflects the geometric extent of the optically thick region rather than the atmospheric column density or mass flux. The existence and location of the saturation boundary are model-independent: they depend only on the product $\sigma(\lambda)\dot{M}$ and the global thermodynamic properties of the wind, and not on the identity of the spectral line, the detailed velocity field, or the specific radiative-transfer implementation. In real systems, the observable geometric extent may be truncated at smaller radii by ionization fronts, interaction with the stellar wind, or Roche-lobe effects.

This result demonstrates that the weak sensitivity of saturated line cores to \dot{M} is not a numerical artifact or a gradual loss of signal, but a direct consequence of the non-invertibility of the optical-depth condition in an expanding atmosphere. Two planets with similar temperature and gravity but substantially different mass-loss rates can therefore exhibit nearly identical saturated line cores, provided that both lie beyond the analytic saturation boundary.

Consequently, strong transmission lines primarily constrain geometric properties of the upper atmosphere, such as the radial extent of the absorbing species and the termination altitude set by ionization or dissociation processes, whereas quantitative constraints on mass loss must rely on opacity-limited diagnostics.

5.3. Connection to the escape parameter and hydrostatic structure

The sonic radius provides a physically transparent link between transmission spectroscopy of winds and classical escape theory. Introducing the Jeans escape parameter evaluated at the planetary radius,

$$\lambda_0 \equiv \frac{GM_p\mu}{kTR_p}, \quad (36)$$

one obtains

$$\frac{r_s}{R_p} = \frac{\lambda_0}{2}. \quad (37)$$

The saturation scale $R_{\text{eff}} \simeq 2r_s$ therefore corresponds to a fixed fraction of the gravitational binding depth of the atmosphere. This highlights a fundamental difference with hydrostatic transmission spectra, in which the effective radius is anchored to an arbitrary reference pressure level. In planetary winds, by contrast, the observable extent of the atmosphere is controlled by the depth of the gravitational potential well and the thermal state of the gas.

5.4. Interpretation in the energy-limited escape framework

Although the analytic solution is expressed in terms of the mass-loss rate, it is instructive to reinterpret the results under the assumption of approximately energy-limited escape,

$$\dot{M}_{\text{EL}} = \frac{\eta\pi R_{\text{XUV}}^3 F_{\text{XUV}}}{GM_p K}, \quad (38)$$

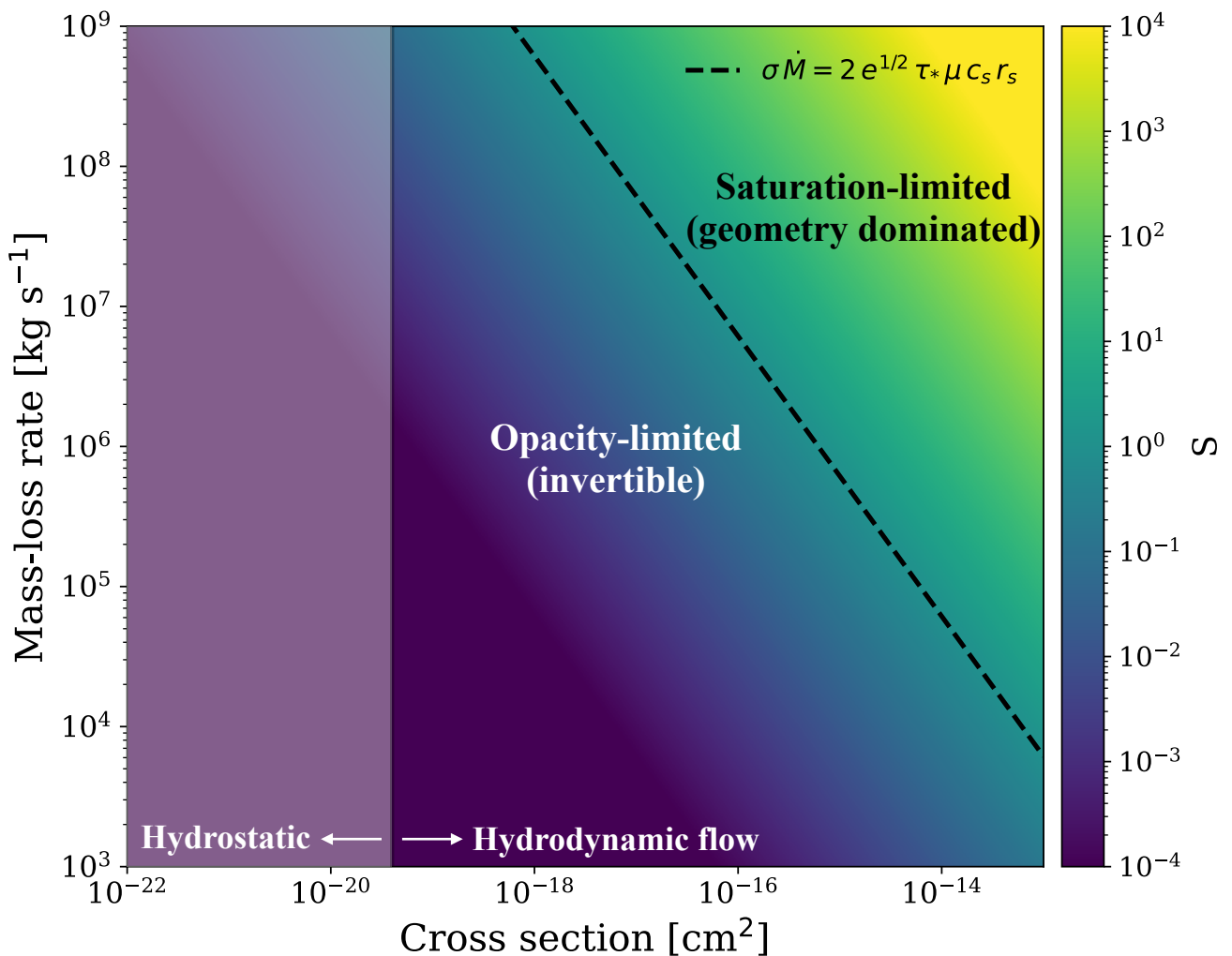


Fig. 6. Regime map for transmission through a hydrodynamic planetary wind, shown in the plane of absorption cross section $\sigma(\lambda)$ and mass-loss rate \dot{M} for HD 209458 b. The color scale represents the dimensionless saturation parameter $S \equiv \sigma(\lambda)\dot{M}/C_{\text{sat}}$, where $C_{\text{sat}} = 2e^{1/2}\tau_*\mu m_p c_s r_s$. The dashed black curve marks the analytic validity boundary $\sigma(\lambda)\dot{M} = C_{\text{sat}}$, separating the opacity-limited regime ($S \ll 1$), in which the transmission depth scales linearly with $\sigma\dot{M}$, from the saturation-limited regime ($S \gg 1$), in which the effective transit radius is set primarily by geometry. The light-gray shaded region indicates cross sections $\sigma \lesssim \sigma_{\text{obs,base}} \sim 4 \times 10^{-20} \text{ cm}^2$, for which absorption becomes optically thin above the XUV heating base and the observed signal is expected to probe below the wind launch region. This figure illustrates the sharp, quantitative boundary between invertible and non-invertible transmission regimes predicted by the analytic model.

where η is the heating efficiency, R_{XUV} the effective absorption radius, F_{XUV} the stellar high-energy flux, and K the Roche-lobe correction factor.

Substituting this expression into the dimensionless control parameter $\chi(\lambda)$ yields the scaling

$$\chi(\lambda) \propto \frac{\sigma(\lambda) \eta F_{\text{XUV}} R_{\text{XUV}}^3 \sqrt{T}}{(GM_p)^2 \mu^{3/2}}, \quad (39)$$

up to numerical factors of order unity. This relation shows that, at fixed opacity, the transmission spectrum of a planetary wind is most sensitive to stellar irradiation and planetary mass, and only weakly dependent on temperature, while retaining a stronger dependence on mean molecular weight through the sound-speed scaling. Within this framework, the analytic saturation boundary can be interpreted as a threshold in stellar forcing beyond which the subsonic region of the outflow becomes optically thick at the wavelengths considered. Strongly irradiated, low-gravity planets are therefore expected to exhibit saturated line cores over wide spectral intervals, whereas higher-gravity or weakly irradi-

ated planets may remain in the opacity-limited regime even for intrinsically strong transitions.

5.5. Implications for observations and retrievals

The analytic results presented here provide a quantitative criterion for assessing the diagnostic power of different spectral tracers of atmospheric escape. Wavelength regions that satisfy the real-domain condition of the Lambert–W solution admit a unique mapping between transmission depth and atmospheric parameters and are therefore suitable for quantitative mass-loss constraints. Regions that violate this condition should instead be interpreted as probes of atmospheric geometry.

This distinction offers practical guidance for observational strategies and retrieval analyses. In particular, it motivates prioritizing weaker transitions and the wings of strong lines when attempting to infer mass-loss rates, and treating saturated line cores as constraints on the spatial extent of the escaping atmosphere rather than on the mass flux itself. More generally, the analytic framework provides a physically transparent complement

to numerical hydrodynamic models, clarifying which aspects of transmission spectra encode information about escape rates and which reflect geometry alone.

Acknowledgements. The author acknowledges financial support from the Severo Ochoa grant CEX2021-001131-S funded by MCIN/AEI/10.13039/501100011033 and Ministerio de Ciencia e Innovación through the project PID2022-137241NB-C43.

Appendix A: Numerical transmission model

We computed fully numerical transmission spectra using the Parker-wind density and velocity profiles. The atmospheric structure was described by a spherically symmetric, isothermal hydrodynamic outflow, for which the radial velocity $v(r)$ and number density $n(r)$ were obtained from the exact Parker solution. The profiles were computed from the planetary radius R_p up to $r_{\max} = 10 R_p$ and were used directly in the radiative transfer calculation.

The wavelength-dependent extinction cross section of the atmosphere was constructed as a volume-mixing-ratio-weighted sum of the individual species cross sections,

$$\sigma_{\text{mix}}(\lambda) = \sum_i x_i \sigma_i(\lambda), \quad (\text{A.1})$$

where x_i denotes the volume mixing ratio of species i . The same mixing ratios as in the analytical models were adopted.

For a given wavelength λ , the chord optical depth at impact parameter b was computed as

$$\tau_\lambda(b) = \int_{-\infty}^{+\infty} n(r(s)) \sigma_{\text{mix}}[\lambda'(s)] \, ds, \quad (\text{A.2})$$

where $r(s) = \sqrt{b^2 + s^2}$ is the radial distance along the line of sight. The Doppler-shifted wavelength $\lambda'(s)$ accounts for bulk hydrodynamic motion and is given by

$$\lambda'(s) = \lambda \left(1 - \frac{v_{\text{los}}(s)}{c} \right), \quad (\text{A.3})$$

with c the speed of light and $v_{\text{los}}(s) = v(r) s/r$ the line-of-sight component of the radial wind velocity. This treatment naturally produces Doppler broadening due to the velocity gradient along the chord, as different regions of the atmosphere contribute at different projected velocities.

Thermal Doppler broadening was included by convolving the mixed cross section $\sigma_{\text{mix}}(\lambda)$ with a Gaussian kernel in $\ln \lambda$, corresponding to a Maxwellian velocity distribution at the atmospheric temperature T_0 . The fractional width of the kernel is $\sigma_{\ln \lambda} = v_{\text{th}}/c$, where $v_{\text{th}} = \sqrt{2k_B T_0/m}$ is the thermal velocity of the absorbing species of mass m .

The wavelength-dependent transit depth was then obtained by integrating over all impact parameters,

$$\delta(\lambda) = \frac{1}{R_\star^2} \left[R_p^2 + 2 \int_{R_p}^{b_{\max}} \left(1 - e^{-\tau_\lambda(b)} \right) b \, db \right], \quad (\text{A.4})$$

where R_\star is the stellar radius and b_{\max} was chosen sufficiently large to enclose the optically thin upper atmosphere.

For resonance lines such as Ly α , the numerical spectra were computed on a high-resolution wavelength grid ($\Delta\lambda \lesssim 10^{-3}$ nm) in order to properly resolve both thermal and bulk Doppler broadening. At coarser wavelength resolution, the impact of velocity broadening on the integrated transit depth is reduced, particularly for optically thick lines.

- Brown, T. M. 2001, ApJ, 553, 1006
 Chubb, K. L., Robert, S., Sousa-Silva, C., et al. 2024, RAS Techniques and Instruments, 3, 636
 Corless, R. M., Gonnet, G. H., Hare, D. E. G., Jeffrey, D. J., & Knuth, D. E. 1996, Advances in Computational Mathematics, 5, 329
 de Wit, J. & Seager, S. 2013, Science, 342, 1473
 Dos Santos, L. A., Vidotto, A. A., Vissapragada, S., et al. 2022, A&A, 659, A62
 Espinoza, N., Steinrueck, M. E., Kirk, J., et al. 2024, Nature, 632, 1017
 Gkouvelis, L. 2025, arXiv e-prints, arXiv:2511.07656
 Gkouvelis, L., Akin, C., & Heng, K. 2024, A&A, 690, A319
 Gkouvelis, L., Gérard, J.-C., Ritter, B., et al. 2018, Journal of Geophysical Research (Planets), 123, 3119
 Gkouvelis, L., Pozuelos, F. J., Drant, T., et al. 2025, A&A, 699, A378
 Heays, A. N., Bosman, A. D., & van Dishoeck, E. F. 2017, A&A, 602, A105
 Koskinen, T. T., Harris, M. J., Yelle, R. V., & Lavvas, P. 2013, Icarus, 226, 1678
 Koskinen, T. T., Yelle, R. V., Lavvas, P., & Lewis, N. K. 2010, ApJ, 723, 116
 Lamers, H. J. G. L. M. & Cassinelli, J. P. 1999, Introduction to Stellar Winds
 Lampón, M., López-Puertas, M., Sanz-Forcada, J., et al. 2023, A&A, 673, A140
 Lecavelier Des Etangs, A., Pont, F., Vidal-Madjar, A., & Sing, D. 2008, A&A, 481, L83
 Linssen, D. C., Oklopčić, A., & MacLeod, M. 2022, A&A, 667, A54
 Murray-Clay, R. A., Chiang, E. I., & Murray, N. 2009, ApJ, 693, 23
 Oklopčić, A. & Hirata, C. M. 2018, ApJL, 855, L11
 Owen, J. E. 2019, Annual Review of Earth and Planetary Sciences, 47, 67
 Owen, J. E., Murray-Clay, R. A., Schreyer, E., et al. 2023, MNRAS, 518, 4357
 Parker, E. N. 1958, ApJ, 128, 664
 Seager, S. & Sasselov, D. D. 2000, ApJ, 537, 916
 Steinrueck, M. E., Savel, A. B., Christie, D. A., et al. 2025, arXiv e-prints, arXiv:2509.21588
 Vidal-Madjar, A., Désert, J.-M., Lecavelier des Etangs, A., et al. 2004, ApJL, 604, L69
 Vidal-Madjar, A., Lecavelier des Etangs, A., Désert, J.-M., et al. 2003, Nature, 422, 143
 Watson, A. J., Donahue, T. M., & Walker, J. C. G. 1981, Icarus, 48, 150

References

- Allan, A. & Vidotto, A. A. 2019, MNRAS, 490, 3760
 Ballabio, G. & Owen, J. E. 2025, Monthly Notices of the Royal Astronomical Society [arXiv:2501.XXXXX]
 Benneke, B. & Seager, S. 2012, ApJ, 753, 100
 Bourrier, V., Lecavelier des Etangs, A., Ehrenreich, D., Tanaka, Y. A., & Vidotto, A. A. 2016, A&A, 591, A121